Coupling atomistic and continuum length scales in heteroepitaxial systems: Multiscale molecular-dynamics/finite-element simulations of strain relaxation in Si/Si$_3$N$_4$ nanopixels

Elefterios Lidorikis,[1,2] Martina E. Bachlechner,[1,3] Rajiv K. Kalia,[1] Aiichiro Nakano,[1] and Priya Vashishta[1]

[1]*Collaboratory for Advanced Computing & Simulations, Department of Physics & Astronomy, Department of Materials Science & Engineering, and Department of Computer Science, University of Southern California, Los Angeles, California 90089*

[2]*Department of Physics, Massachusetts Institute of Technology, Cambridge, Massachusetts 02139*

[3]*Physics Department, West Virginia University, Morgantown, West Virginia 26506*

A hybrid atomistic-continuum simulation approach has been implemented to study strain relaxation in lattice-mismatched Si/Si$_3$N$_4$ nanopixels on a Si(111) substrate. We couple the molecular-dynamics (MD) and finite-element simulation approaches to provide an atomistic description near the interface and a continuum description deep into the substrate, increasing the accessible length scales and greatly reducing the computational cost. The results of the hybrid simulation are validated against full multimillion-atom MD simulations. We find that strain relaxation in Si/Si$_3$N$_4$ nanopixels may occur through the formation of a network of interfacial domain boundaries reminiscent of interfacial misfit dislocations. They result from the nucleation of domains of different interfacial bonding at the free edges and corners of the nanopixel, and subsequent to their creation they propagate inwards. We follow the motion of the domain boundaries and estimate a propagation speed of about $\sim 2.5 \times 10^3$ m/s. The effects of temperature, nanopixel architecture, and film structure on strain relaxation are also investigated. We find: (i) elevated temperature increases the interfacial domain nucleation rates; (ii) a thin compliant Si layer between the film and the substrate plays a beneficial role in partially suppressing strain relaxation; and (iii) additional control over the interface morphology may be achieved by varying the film structure.

I. INTRODUCTION

Semiconductor heteroepitaxy is of great technological value and promise for the fabrication of interesting electronic and optoelectronic devices.[1] Such devices contain overlayers and/or buried elements of materials whose lattice constants are generally different from those of the substrate. These layers are thus grown in a strained state causing large stresses that extend throughout the device. Since strain alters the electronic band structure of the semiconductor materials, it is possible to exploit the lattice mismatch to fabricate devices with tailored electronic and optical properties.

When a heteroepitaxially grown film exceeds a certain critical thickness,[2–10] the mismatch strain may be relaxed via two classes of mechanisms, depending on whether or not they destroy the interface coherence. The coherent mechanisms are typically observed in systems with large (greater than a couple of percent) mismatch, and include morphological instabilities such as ripples and island formation, resulting in a three-dimensional (3D) growth-mode.[11–14] The incoherent mechanisms, on the other hand, are observed in systems with small mismatch, and involve formation of interfacial defects such as misfit dislocations and/or dislocation arrays, which, however, do not destroy the planar morphology of the film, resulting in a layer-by-layer 2D growth-mode.[6,15–20] In cases of very large mismatch both classes of mechanisms may become operative. While strain relaxation processes destroy the uniformity of the strain fields and thus their beneficial role in some device applications, they can have a desirable effect in other applications such as in assisting the self-organization of 3D islands in order to form regular arrays of quantum dots.[11,21] In any case, the understanding of the relaxation mechanisms and the conditions under which they become operative is an important step towards intelligent control over the growth process of such lattice-mismatched systems.

Traditional analytical and computational approaches based on elasticity theory treat the mismatched film-substrate system as a continuum, decomposing the energy into bulk, surface, and interface contributions.[3–8,12,14,22–27] Such a continuum description is important in order to capture the effects of the long-range stress fields that are the driving force of strain relaxation. If the interface energetics and strain relaxation mechanisms are known, these approaches can provide a valuable description of equilibrium strains and shapes of such systems. Which mechanism is dominant in a particular case, however, depends on the atomic structure of the film-substrate interface and thus can only be determined by an atomistic description.[28–34] A fully atomistic approach, on the other hand, can only be applied to systems of limited size. Since it ignores the long-range part of the stress field, a direct comparison with experiment becomes problematic. This is a multiscale problem: nucleation and evolution of misfit dislocations takes place inside a limited region around the heterostructure interface and should be described by an atomistic method, while the elastic strain energy that drives this process is distributed macroscopically throughout the structure where a continuum method suffices for its description.

Recently developed multiscale simulation approaches[35–41] utilize the molecular dynamics (MD) and the finite element (FE) methods for the atomistic and continuum descriptions, respectively. There are two types of atomistic-

continuum simulation approaches. In one type, formally formulated by Abraham, Broughton, Bernstein, and Kaxiras,[39] the system is separated in two regions, one described by MD and the other by FE, while a hand-shaking scheme is defined for the FE-MD interface.[35,36,39,41] In the other approach, formulated by Tadmor, Ortiz and Phillips,[37] the FE formulation is retained throughout the system, while MD is used to define the corresponding continuum constitutive relations.[37,40]

In this paper, we implement the multiscale simulation approach of the first type, to study the multiscale problem of strain relaxation. We have applied this approach to study a Si/Si_3N_4 nanopixel on a $Si(111)$ substrate, which is potentially important in microelectronics. Recent experiments and simulations have shown a 2D growth mode for such systems,[31,42,43] however, little is known about the strain relaxation mechanisms. The small lattice mismatch($\sim 1.25\%$) requires large simulation systems in order for the relaxation mechanisms to become operative. We will use the MD method in the Si_3N_4 film and Si/Si_3N_4 interface region, and a continuum description (FE) of the Si substrate below the interface region, for a pixel of lateral size 50×50 nm^2. Since MD can provide complete space-time trajectories of atoms at finite temperature, we will be able to follow the nucleation and dynamic evolution of the strain relaxation mechanisms. By varying initial conditions such as temperature, pixel architecture, and film structure, we will be able to draw conclusions on ways to control the strain relaxation processes.

The paper is organized as follows. In Sec. II we provide an introduction to strain relaxation processes and issues of current research in semiconductor heteroepitaxy, focusing mainly on systems that exhibit a 2D growth mode. An introduction to existing computational modeling approaches of such systems as well as to multiscale simulation approaches is also discussed in this section. In Sec. III we outline, test, and validate the MD-FE multiscale simulation approach that we will use for the nanopixel problem. In Sec. IV we provide a description of the symmetries and energetics of the nanopixel system and an outline of the multiscale simulation strategy, followed by the simulation results, which include the strain relaxation nucleation and evolution as well as the effects of temperature, pixel architecture, and film structure. Finally, in Sec. V we summarize our main conclusions.

II. PRELIMINARIES

One of the first questions formulated in the field of strain relaxation in heterostructures was the conditions that drive a coherently strained film to relax via formation of misfit dislocations. These misfit dislocations lay on the film-substrate interface and their Burgers vector is such as to relieve some of the mismatch strain. Van der Marwe in 1962 (Ref. 2) estimated a critical film thickness that marks the onset of such misfit dislocation nucleation. His approach was based on energy considerations: at the critical film thickness h_c the interfacial energy between the film and the substrate (which is the energy available for dislocation generation) equals the mismatch strain energy. Matthews and Blakeslee[3] used force equilibration considerations. Assuming a pre-existing dislo-

cation, there are two opposite forces applied to it: one is the tension in the dislocation line that depends on the film thickness, and the other is due to the mismatch strain. If the mismatch force is equal or larger compared to the tensile force, the formation of the misfit dislocation is favorable, and an expression for the critical film thickness is derived accordingly. An improved energy condition was later provided by People and Bean:[5] the areal strain energy density due to mismatch exceeds the self-energy of an isolated dislocation for films thicker than h_c. This produced the best agreement with experimental results on a Ge_xSi_{1-x}/Si system.[4] Further advancements include the work of Hirth and Feng,[8] who calculated the critical layer thickness for misfit and inclined dislocation stability in strained multilayer structures, and that of Freund and Nix,[7] who generalized the Matthews and Blakeslee criterion to the case of a compliant (i.e., finite thickness) substrate, among many others.[44,23,9,45] The kinetics of these misfit dislocations has also been studied by a number of researchers.[45–47,27]

On the experimental side, Tsao *et al.*[6] studied Si_xGe_{1-x} layers grown on Ge and concluded that the stress, which actually drives dislocation motion, is the difference between the usual stress due to misfit strain and an "effective" stress due to dislocation-line tension. Observable strain relief occurs only if this "excess" stress exceeds a critical value, which, however, depends on temperature. Lee *et al.*[15] used ballistic electron emission microscopy (BEEM), atomic force microscopy (AFM), transmission electron microscopy (TEM) and scanning tunneling microscopy (STM) on InGaAs/GaAs interfaces, and found cross-hatch patterns that originate from misfit dislocations. Belk *et al.*[16] used STM to study misfit-dislocation induced lattice distortions of the epilayer for InAs thin films grown on GaAs(110). 2D islands with regular size are observed when two monolayers (MLs) of InAs are grown. Upon further growth, interfacial misfit dislocations appear following the coalescence of the 2D islands. The growth mode remains 2D for all coverages. Yamaguchi *et al.*[17] studied strain relaxation in InAs/GaAs(111)A heteroepitaxy on the atomic scale by STM. The coalescence of small islands and the formation of a dislocation network are identified at the critical layer thickness (~ 2 MLs), and no 3D growth is observed for all coverages. The measured density of the misfit dislocations indicates that the strain is not fully relaxed at the critical layer thickness, but is instead gradually relieved with the additional growth of InAs. Ohtake and Ozeki[10] performed *in situ* measurements of strain in the surface-normal direction during InAs/GaAs(111)A heteroepitaxy. They found that the initially grown InAs lattice (≤ 3 MLs) is under compressive strain in the surface-normal direction as well as in the surface-parallel direction, contrary to the prediction of elastic theory. By changing the film composition $In_xGa_{1-x}As$, they observed that the strain relaxation in the surface-normal direction hardly depends on the degree of the lattice mismatch, in marked contrast to the in-plane case. Their conclusion is that elastic theory can adequately be applied to InAs films thicker than 20 MLs. Wiesauer and Springholz[48] have found experimentally that misfit dislocation interactions in PbTe on PbSe(001) can significantly lower the kinetic barriers and thus increase the rate of relaxation.

A promising approach to controlling the strain relaxation mechanisms, and thus the quality of the epitaxial film, relies on the utilization of compliant substrates. A compliant substrate is mechanically similar to a finite-thickness substrate unconstrained at its base, so that it can laterally relax in order to accommodate part of the mismatch strain, inhibiting the formation of misfit dislocations and other morphological instabilities. Luryi and Suhir[49] proposed the use of a patterned substrate in the form of small seed pads. They showed that the free space between the pads is used for lateral expansion that relieves the mismatch strain, and calculated the critical pad size below which, for a given mismatch, thick films can be grown without misfit dislocations. Powell, Iyer, and LeGoues[50] proposed and experimented on depositing SiGe on a thin layer of Si, which in turn is on a SiO_2 wafer. The Si layer slides on the amorphous SiO_2 and thus shares the mismatch strain. As the GeSi film grows thicker, more strain is accommodated by the Si film, while any plastic deformation or dislocation formation happens inside the Si film, leaving the GeSi film relaxed and free of defects. Ejeckam *et al.*[51] employed twist-wafer bonding to help achieve the desired lattice compliance properties. A large twist angle introduces a dense square array of screw dislocations between the bulk substrate and the thin film. Because of them, the film becomes very flexible, playing thus the role of the compliant substrate. The physical origin of the observed compliance in twist-wafer bonding is still an object of debate.[52–54] Another approach is the use of an intermediate layer between the film and the substrate. Nakada *et al.*[42] successfully grew high quality GaN films on Si(111) substrates through the formation of amorphouslike silicon nitride layers with thickness of about 1–1.5 nm on the Si surface, while Wang *et al.*[43] achieved the growth of crystalline $Si_3N_4(0001)$ on Si(111) by exposing the Si substrate to nitridation gases. These approaches show that it may be possible to fabricate new optoelectronic devices by combining GaN growth techniques with already well-established silicon device technology.

From the above introduction it is apparent that there are still great challenges in this technologically important field. Computational approaches will play a significant role in advancing our atomistic understanding, by making it possible to study regions unreachable by analytic theory (realistic finite sizes and geometries, compliant layers, interface chemistry, temperature, etc.), as well as providing a link between theoretical approaches and experiment. The remainder of the section presents a simple energetic consideration of the strained film problem, existing computational continuum and atomistic approaches, and previous multiscale simulation approaches.

A. Continuum elasticity theory

We will formulate here an elementary linear elastic description[55] of the general heterostructure problem. For this, we consider a simplified one-dimensional model of a film-substrate system: a finite-thickness isotropic film deposited on a finite-thickness isotropic substrate, both being infinite in the other two lateral dimensions. The top of the film and bottom of the substrate surfaces are assumed free. We denote
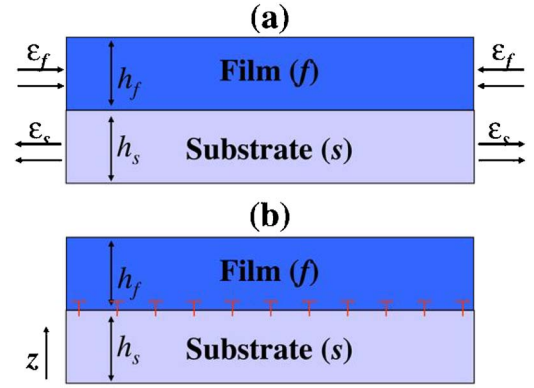

FIG. 1. (Color online) Schematic of a mismatched film-substrate system: (a) fully strained and (b) fully relaxed through interfacial misfit dislocations.

the film and substrate thicknesses as h_f and h_s, their shear moduli and Poisson's ratios as μ_f, ν_f and μ_s, ν_s, and their equilibrium atomic lattice constants as a_f and a_s, respectively. We assume that $a_f > a_s$. We will consider two cases: (i) coherently strained film/substrate system, (ii) fully relaxed film-substrate system via formation of interfacial misfit dislocations.

In the coherently strained case [Fig. 1(a)] film and substrate are under biaxial compressive and tensile strains ε_f and ε_s, respectively, with $\varepsilon_f - \varepsilon_s = \varepsilon_m = (a_s - a_f)/a_f$. The corresponding biaxial stresses are $\sigma_f = M_f \varepsilon_f$ and $\sigma_s = M_s \varepsilon_s$, where $M_i = 2\mu_i(1+\nu_i)/(1-\nu_i)$ for $i = f, s$. The total elastic strain energy per unit area is $V_{coherent} = M_f \varepsilon_f^2 h_f + M_s \varepsilon_s^2 h_s$, while the equilibrium film strain and the equilibrium energy per unit area are

$$\varepsilon_f = \frac{\varepsilon_m}{1 + M_f h_f / M_s h_s}, \quad V_{coherent} = \frac{M_f \varepsilon_m^2 h_f}{1 + M_f h_f / M_s h_s}. \quad (1)$$

In the limit of infinitely thick substrate, $h_s \to \infty$, the total mismatch strain is accommodated solely by the film $\varepsilon_f = \varepsilon_m$ and the elastic energy becomes $V_{coherent} = M_f \varepsilon_m^2 h_f$.

In the fully relaxed case [Fig. 1(b)], a regular array of interfacial misfit dislocations is introduced at the interface, eliminating the mismatch strain. Assuming these are edge dislocations, we may estimate a Burgers vector of magnitude $|\vec{b}| = a_s$ and so an average interdislocation separation distance of $\langle d \rangle = a_s / \varepsilon_m$, which yield an average dislocation density of $\langle N \rangle = 2/\langle d \rangle$ (the factor of 2 is for the two perpendicular directions). We have assumed here that the dislocations are self-organized into a regular square array, but this may vary depending on the underlying atomic lattice structure and possible slip directions. The total potential energy now consists of the dislocation core energy, the dislocation elastic self-energy, the dislocation interaction with the free surfaces, and the dislocation-dislocation interactions. Ignoring the last part, we have for the potential energy per unit area $V_{relaxed} = \langle N \rangle [V_{elastic} + V_{core}] + \gamma_{sf}$, where V_{core} is the interatomic energy due to the atomic lattice distortion in the dislocation core and γ_{sf} is the stacking fault energy that may result at the interface due to the deformation introduced by the disloca-

tion. Both of these terms are atomistic in nature. $V_{elastic}$ describes the energy of the dislocation's strain fields including their interaction with the free surfaces,

$$V_{elastic} = \frac{\mu_{eff}|\vec{b}|^2}{4\pi(1-\nu_{eff})}(1-\nu_{eff}\cos^2\theta)\ln\left|\frac{h_f h_s}{|\vec{b}|(h_f+h_s)}\right|, \quad (2)$$

where μ_{eff} and ν_{eff} are the corresponding effective shear modulus and Poisson's ratio, which describe a film-substrate system that is treated as a single effective medium, and θ is the angle between the Burgers vector and the dislocation line (in our case of edge dislocations $\theta = \pi/2$).

In a realistic case, the equilibrium is a mixture of the coherently strained and the fully relaxed cases. Furthermore, in realistic finite-width cases, the situation is even more complicated. The free-surface energies must enter the equations explicitly and so the equilibrium now depends on the surface-to-volume ratios, introducing such effects as bending or buckling. Corners and edges should also be taken into account. Depending on the underlying atomic lattice symmetries and slip directions, the dislocation's Burgers vectors and dislocation lines, as well as their arrangement, may be different. In some cases, they may split into partials, which, for example, introduce stacking faults at the interface. A continuum description of such systems, using a numerical technique such as the finite element method, assumes that all of the above energies and mechanisms are known. This requires complete understanding of the materials properties of film and substrate, as well as their interface atomic structure. If this is not the case, then the molecular-dynamics method is required to obtain an atomistic description of the system.

B. Review of computational approaches

Most computational approaches that solve the continuum elasticity equations use the finite element method. Examples include the work of Jain *et al.*[22] who calculated the stresses and strains in mismatched substrates and stripe films of any thickness and width, Johnson and Freund[23] who calculated the equilibrium shapes of strained islands on a substrate as a function of mismatch and island volume, and Zhuang *et al.*,[24] who calculated displacements in Si/SiGe quantum wires. A great advantage of this method is that it enables the simulation of structures of realistic size, providing a direct link with the experimental data. For example, Pinardi *et al.*[56] and Zhuang *et al.*[24] used the calculated strains to reproduce previously measured Raman spectra and x-ray-diffraction patterns respectively, thereby providing a quantitative interpretation of the experimental data. The disadvantage of this computational approach, however, is its rather limited predictive capability. Equilibrium bulk and surface material properties are assumed, despite the fact that these may change in regions of high deformations.[32,18] Continuum elasticity may not even be valid in the case of ultrathin ($\sim$3-ML) films.[10] Strain relaxation mechanisms such as nucleation of misfit dislocations cannot be predicted *a priori*, and even if they are known, they are much more suitably described by an atomistic approach since they are atomistic in nature.

Atomistic simulation approaches utilizing the molecular-dynamics method circumvent these problems by directly dealing with the discrete character of the system under study. Using reliable interatomic potentials, all material properties such as symmetries, interface interactions, nonlinear and/or plastic deformation responses are built into the MD scheme. Zhang and Lagally[28] studied the use of foreign atoms at the interface as means of an alternate strain relaxation mechanism to suppress the 2D-to-3D growth mode transition. Zepeda-Ruiz *et al.*[18] studied the energetics of misfit dislocation formation as well as the variation of the critical thickness as a function of the substrate's compliance for InAs/GaAs heteroepitaxial systems. Yu and Madhukar[29] studied the behavior of energetics and atomically resolved stresses and strains of Ge islands on Si (see also Refs. 33 and 34), while Cusack *et al.*[30] studied pyramidal InAs dots on GaAs (see also Ref. 32). Su *et al.*[57] identified growth limiting mechanisms in InAs/GaAs dots, thereby interpreting some recent experimental results,[58] and Bachlechner *et al.*[31] found highly inhomogeneous stress distributions in Si/a-Si$_3$N$_4$ nanopixels. Direct comparisons with experiments were done by Nosho *et al.*[59] who used STM and MD simulations to study the surface morphology and interfacial stability in InAS/GaAS(111)A heteroepitaxy and found good agreement between simulation and experiment. Simulations of epitaxial growth were performed by Jacobsen *et al.*,[60] who combined kinetic Monte Carlo and MD to achieve simulation times of seconds. They studied energetic beam deposition and found the energetic conditions for layer-by-layer growth.

The simulation results mentioned above show the great promise and potential of atomistic approaches. As computer power increases, larger and more realistic systems can be simulated to provide insight and in some cases direct interpretation of experimental data. One area, though, that has not been extensively studied is the actual dynamics of the strain relaxation mechanisms; the nucleation and dynamical evolution of the misfit dislocations in systems of realistic size and temperature. An atomistic description of such a system, however, is limited due to computational constrains, to the study of zero-temperature structural relaxation and energetics. Here we will use a computational scheme that brings together the atomic resolution needed at the interface, with the continuum description of larger length scales needed to reach the experimental sizes, and will study the multiscale problem of strain relaxation dynamics. In the next subsection, we provide a brief overview of existing multiscale computational approaches, one of which we will choose to study our system.

C. Review of multiscale computational approaches

One of the first multiscale simulations to couple atomic and continuum elasticity dynamics is the two-dimensional embedded atom approach of Mullins *et al.*,[35] who used it to study the (001) plane crack in α-iron. The idea is to create a region surrounding the crack tip where MD is used to provide the necessary atomic resolution, which is embedded in a larger macroscopic region described by a continuum approach. In this larger region the equations of linear elasticity are solved on a computational grid by using the FE method. The handshaking between the two regions is done as follows:

inside the grid cells (elements) that are at the interface of the two regions, pseudoatoms that interact with the real atoms *via* the interatomic potential are embedded. The atomic forces that are exerted on them are transferred to the grid points (nodes) of the corresponding elements through use of interpolation functions. Thus the new deformation state of the continuum system is directly affected by the atomic interactions. The embedded atoms, in turn, move in lock position with the continuum, and so through their interaction with the real atoms, the information about the new deformation state is passed back to the MD region. This "handshaking" scheme was an early dynamic coupling of the two length scales.

An improved coupling scheme was later introduced by Kohlhoff *et al.*[36] who studied crack propagation in bcc crystals. Instead of just bringing together the FE and atomic regions, the FE grid close to the interface was scaled down to the atomic size and forced to overlap over a wide "transition zone," establishing a one-to-one correspondence between the atoms and the nodes. This scheme ensured that all atomic and nodal forces were calculated using a complete set of neighbors, providing therefore a smoother coupling between MD and FE. A further improvement was introduced by Abraham *et al.*,[39] when they defined an explicit Hamiltonian for the transition zone, in a full three-dimensional application for fracture in silicon: the hybrid particles close to the handshake surface follow hybrid (i.e., averaged over MD and FE) dynamics. This ensures a seamless transition between the two length scales and well-defined energy conserving dynamics. Finally, in the coarse-grained molecular-dynamics method of Rudd and Broughton,[40] the constitutive relations for continuum are improved, by deriving them directly from the interatomic potential by means of a statistical coarse graining procedure. For atomic size elements, the atomic and nodal degrees of freedom are equal in number, and thus we get the same dynamics, while for large elements we recover the continuum elasticity equations of motion. This method constitutes the highest quality coupling of the two length scales.

A different and very successful multiscale simulation approach for coupling atomistics with continuum is the quasi-continuum method of Tadmor *et al.*[37] Here, the FE formulation is retained throughout all space. The potential energy of each element, however, is not defined through the continuum elasticity constitutive relations, but rather, through a separate atomistic calculation using the actual microscopic interatomic potential. Within each element we assign a representative crystallite of the actual material, deformed according to the local deformation inside the element. The calculated microscopic potential energy is assigned as the energy of that element. In areas of high deformation, the grid is adaptively refined. Once all energies are calculated, the system is brought to equilibrium by means of a zero-temperature energy-minimization process. The advantage of this method is its ease to simulate complex structure such as dislocations and defects. It has been successfully used for many studies, such as the interactions between grain boundaries, dislocations and cracks,[61] or nanoindentation,[62] etc. There are several review articles on the various multiscale issues and methodologies for a variety of physical problems.[63–66]

For the problem of strain relaxation, the concurrent coupling of length scales method of Abraham *et al.*[39] is the most attractive one. The existence of an explicit Hamiltonian for the entire system ensures energy conservation, which is crucial for a realistic description of dynamics at a finite temperature. Furthermore, the basic limitation of this method, i.e., the handshake between MD and FE is in a fixed region of space, excluding the possibility for adaptive re-meshing. The region in which dislocations evolve, and thus must be described atomistically, is around the interface and is fixed. Finally, the computational efficiency of this scheme is very high. In the next section we describe our implementation of the concurrent coupling of length scales, which includes a few modifications from the original methodology in order to improve the coupling in the handshake region as well as the overall computational efficiency.

III. METHODOLOGY FOR CONCURRENT COUPLING OF LENGTH SCALES

Recently, Abraham, Broughton, Bernstein, and Kaxiras[39] developed a Hamiltonian formulation of a hybrid simulation approach that combines large-scale molecular-dynamics (MD) simulations embedded in a continuum, which is handled with the finite element (FE) approach based on linear elasticity. First, the physical system is spatially divided into FE, MD, and handshake (HS) regions. Within the FE region, the equations for continuum elastic dynamics are solved on a FE mesh. To make the transition from the FE to MD regions seamless, the FE mesh in the HS region is refined down to the atomic scale near the FE-MD interface in such a way that each FE node coincides with an MD atom, establishing a one-to-one correspondence between the atoms and the nodes. These hybrid node-atoms follow hybrid dynamics to ensure a smooth transition between the FE and MD regions. An explicit energy function, or Hamiltonian, for this HS zone is defined to ensure energy-conserving dynamics. We will follow here their scheme, introducing modifications in order to improve the quality of the FE-MD coupling.

A. Molecular dynamics method

In MD simulations, the physical system is described by sets of N atomic positions $\{\vec{r}_i | i = 1, \ldots, N\}$ and velocities $\{\vec{v}_i | i = 1, \ldots, N\}$. We discretize time into discrete intervals Δt and numerically solve Newton's equations of motion with an interatomic potential $V_{MD}(\{\vec{r}_i\})$. In our MD simulations, the interatomic potential consists of two- and three-body terms, $V_{MD} = \Sigma_{(i,j)} V_{ij}^{(2)}(\vec{r}_i, \vec{r}_j) + \Sigma_{(i,j,k)} V_{ijk}^{(3)}(\vec{r}_i, \vec{r}_j, \vec{r}_k)$. To simulate Si/Si_3N_4 systems, the interatomic potential should be able to describe these very different materials as well as the interface in a seamless fashion. In our model, we have to distinguish between Si atoms in the silicon crystal and in silicon nitride. In addition, the atoms at or near the interface have different charge transfer and therefore have to be treated differently. Based on linear combination of atomic orbitals (LCAO) electronic structure calculations for the

Si(111)/Si₃N₄(0001) interface, we find that the Si/Si$_3$N$_4$ system may be adequately modeled as an eight-component system, where each of the eight atom types is associated with a different set of parameters in the interatomic potential. The different types of atoms are as follows: in the silicon nitride bulk we have 1 Si atom and 1 N atom. On the silicon nitride surface we have 1 Si atom and 2 N atoms (one twofold and one threefold coordinated). In the silicon bulk we have 1 Si atom and on the Si surface we have 2 Si atoms (one threefold and one fourfold coordinated on the top and second atomic layer, respectively).[70] To model bulk Si, we have chosen the Stillinger-Weber (SW) potential[67] which provides a reasonable description of crystalline silicon. The potential for bulk silicon nitride is constructed from two- and three-body terms.[68] The two-body part contains the effects of charge transfer, electronic polarizability, and steric repulsion, while the three-body covalent terms represent the effects of bond bending and stretching. This interatomic potential has been validated by comparison with experimental properties of crystalline and amorphous Si$_3$N$_4$.[69] For atoms at the interface, the charge transfer, bond lengths, and bond angles are consistent with the results of the electronic structure calculations.[70]

B. Finite element method

Under the action of applied forces, solid bodies undergo deformations such as changes in shape and volume. For a given deformation, the position $\vec{r}$ of any point is displaced to a new position $\vec{r}'$, defining the displacement vector for that point $\vec{u}(\vec{r}) = \vec{r}' - \vec{r}$. In the limit of linear elasticity (which we use in this work), the strain at the point $\vec{r}$ is defined as $\varepsilon_i(\vec{r}) = \partial u_i(\vec{r})/\partial r_i$ and the shear as $\gamma_{ij}(\vec{r}) = (\partial u_i(\vec{r})/\partial r_j + \partial u_j(\vec{r})/\partial r_i)$, where $i,j = 1,2,3$ denote the three orthogonal directions. In the absence of tractions and body forces, the total elastic energy of a solid is given by

$$H_{FE} = V_{FE} + K_{FE} = \frac{1}{2}\int \{\varepsilon\}^T[E]\{\varepsilon\}d\Omega + \frac{1}{2}\int \rho|\dot{\vec{u}}|^2 d\Omega, \quad (3)$$

where $\{\varepsilon\}^T = \{\varepsilon_1, \varepsilon_2, \varepsilon_3, \gamma_{12}, \gamma_{23}, \gamma_{13}\}$, $[E]$ is the reduced 6×6 elastic moduli matrix, $\rho = \rho(\vec{r})$ is the mass density, and $\dot{\vec{u}} = \dot{\vec{u}}(\vec{r})$ is the rate of change of the displacement field. The stress at a point $\vec{r}$ is $\{\sigma\} = \{\partial V_{FE}/\partial \varepsilon\} = [E]\{\varepsilon\}$, while the restoring force opposing the deformation $f_i(\vec{r}) = \partial V_{FE}/\partial u_i|_r$.

In the finite element method[71] we discretize the solid into a grid. The continuous displacement field $\vec{u}(\vec{r})$ is defined at the grid points (nodes) and interpolated within the grid cells (elements). We denote the nodal displacements as $\{\vec{D}\} \equiv \{\vec{D}_i\}$ for $i = 1, N$ where N is total number of nodes (grid

points). If we "pull out" from $\{\vec{D}\}$ the nodal displacements of a specific element, we form the elemental displacement vector $\{\vec{d}\} \equiv \{\vec{d}_i\}$ for $i = 1, n$ where n is now the number of nodes in that element. In a similar way we define the nodal velocity and acceleration $\{\dot{\vec{D}}\}, \{\ddot{\vec{D}}\}$ and the corresponding elemental vectors $\{\dot{\vec{d}}\}, \{\ddot{\vec{d}}\}$.

Interpolation within each element is done using an isoparametric formulation. This allows us to generate nonrectangular elements, which is useful in transitioning from a coarse to a fine grid. Isoparametric signifies that we use the same parameters and interpolation scheme for any field that is interpolated from its nodal values (e.g., displacements, coordinates, etc.). Isoparametric elements are always defined in "natural" coordinates (ξ, η, ζ), where $-1 \leq \xi, \eta, \zeta \leq +1$. We define the linear interpolation functions (also called shape functions) $N_i(\xi, \eta, \zeta)$ [e.g., for an eight-node element they are $N_i(\xi, \eta, \zeta) = \frac{1}{8}(1 \pm \xi)(1 \pm \eta)(1 \pm \zeta)$], so that any field Φ can written as $\Phi(\xi, \eta, \zeta) = \Sigma_{i=1}^n N_i(\xi, \eta, \zeta)\Phi_i$, where Φ_i are its nodal values. The shape functions satisfy $N_i(\xi^j, \eta^j, \zeta^j) = \delta_{ij}$ and $\Sigma_{i=1}^n N_i(\xi, \eta, \zeta) = 1$.

The interpolation of the elemental displacement vector is written in compact notation as $\{\vec{u}\} = [N]\{\vec{d}\}$. From this we calculate the strain $\{\varepsilon\} = [\partial_{real}]\{\vec{u}\} = [J]^{-1}[\partial_{natural}][N]\{\vec{d}\}$ $= [B]\{\vec{d}\}$ where we defined the Jacobian transformation $[J] = \partial x(\xi, \eta, \zeta)/\partial \xi = \Sigma_{i=1}^n N_{i,\xi}(\xi, \eta, \zeta)x_i$, where x_i are the nodal coordinates (for more details, see Ref. 71).

The elastic potential energy is now defined as

$$V_{FE} = \frac{1}{2}\int_\Omega \{\varepsilon\}^T[E]\{\varepsilon\}d\Omega = \frac{1}{2}\sum_{l=1}^{N_{elements}} \{\vec{d}\}_l^T[k]_l\{\vec{d}\}_l, \quad (4)$$

where $[k]_l = \int_{\Omega_l} [B]_l^T[E]_l[B]_l d\Omega_l$ is the stiffness matrix of element l. In a similar manner we calculate the kinetic energy

$$K_{FE} = \frac{1}{2}\int_\Omega \rho(\vec{r})|\dot{\vec{u}}(\vec{r})|^2 d\Omega = \frac{1}{2}\sum_{l=1}^{N_{elements}} \{\dot{\vec{d}}\}_l^T[m]_l\{\dot{\vec{d}}\}_l, \quad (5)$$

where $[m]_l = \int_{\Omega_l} [N]_l^T\rho(\vec{r})[N]_l d\Omega_l$ is the mass matrix of element l. For the evaluation of $[k]_l, [m]_l$ we use the Gauss quadrature integration rule. Finally, assuming external loads $\{\vec{R}\} \equiv \{\vec{R}_i\}$ for $i = 1, N$ at the structure's nodes, whose work is $-\{\vec{D}\}^T\{\vec{R}\}$, then in the equivalent global notation the total energy is written as

$$E = \frac{1}{2}\{\vec{D}\}^T[K]\{\vec{D}\} + \frac{1}{2}\{\dot{\vec{D}}\}^T[M]\{\dot{\vec{D}}\} - \{\vec{D}\}^T\{\vec{R}\} \quad (6)$$

and the equations of motion

$$[M]\{\ddot{\vec{D}}\} = -[K]\{\vec{D}\} + \{\vec{R}\}, \quad (7)$$

where $[K]$, $[M]$ are the system's global stiffness and mass matrix, respectively, formed by the corresponding elemental
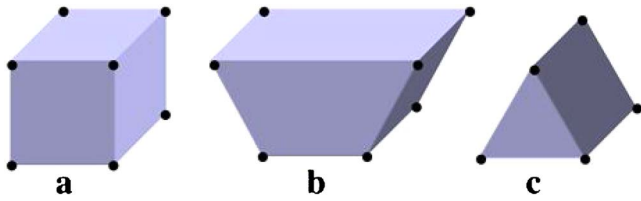
FIG. 2. (Color online) The three element shapes used in fine graining the FE grid.

ones $[K] \leftrightarrow \Sigma_{l=1}^{N_{elements}}[k]_l$ and $[M] \leftrightarrow \Sigma_{l=1}^{N_{elements}}[m]_l$.

The mass matrix $[m]$ is nondiagonal, representing a continuous mass distribution. In the case of small, atomic-size elements, however, this turns to be a bad approximation, since mass is not continuously distributed in space but rather discretely assigned at the atomic lattice positions. A better approach is to use the lumped mass approximation, in which the mass is assigned only to the nodes and thus $[M]$ becomes diagonal. This is particularly convenient since we avoid the evaluation of $[M]^{-1}$. Furthermore, the calculation of the acceleration can then be done element by element, avoiding the construction of the global $[K]$. These considerations reduce the problem's computational complexity to $O(N)$.

In our application we will use FE to simulate crystalline silicon. Since the FE silicon will be ultimately interfaced with MD silicon, it is imperative to use a consistent description across the two regions. The MD silicon is described by the Stillinger-Weber (SW) (Ref. 67) interatomic potential, and thus we choose to use the elastic constants of silicon that are predicted by the SW potential as opposed to using the corresponding experimental values. We will thus use the values 151.5, 76.5, and 56.5 GPa for C_{11}, C_{12}, and C_{44} respectively.

C. Handshaking of atomistic and continuum regions

The characteristic length scales of the atomistic and continuum systems are inherently different. The atomistic system's length scale is invariably set by the bond lengths and is the same throughout the system. The continuum system's length scale, on the other hand, is set by the size of the finite elements used, and it can vary within the system. If we wish to couple these two systems together, we need to create a region of space in which their characteristic length scales will match, i.e., a region in which the finite element grid is fine grained down to the atomistic dimensions.

To achieve this we use three different basic element shapes, shown in Fig. 2. Element (c) uses a different interpolation scheme (i.e., shape functions) than (a) and (b) do, being a six-node element instead of an eight-node one. Assuming the direction towards the MD region is the z direction, then fine graining is done first in the x and z directions, then in the y and z directions, and the cycle continues until we reach the atomic dimensions. In each cycle we reduce each dimension by a factor of 2. At the edges of the x, y directions, the elements wrap around and periodic boundary conditions are applied.

After reaching the atomic dimensions, we couple the FE grid with the MD lattice. The best strategy follows an
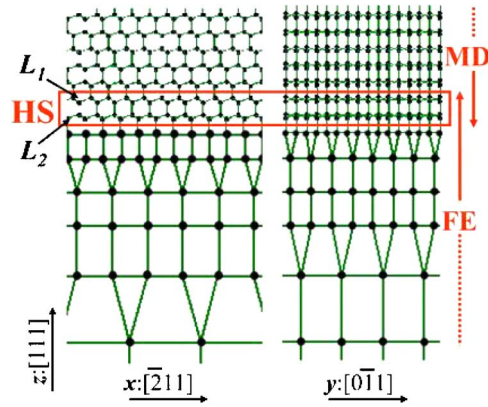

FIG. 3. (Color online) Two projections of the 3D MD-HS-FE grid for Si(111). For the MD region we use the Stillinger-Weber potential, which involves nearest-neighbor atoms, and only two atomic bilayers are needed to be within the HS region.

idea due to Kohlhoff *et al.*[36] which calls for a finite region in space in which the MD lattice overlaps with the FE grid in such way that the MD atomic positions coincide with the FE nodal positions. To do so, the FE grid in this region is shifted from cubic into a structure that exactly follows the atomic lattice. These hybrid atom-node particles constitute the handshake region. The width of the HS region is set by the longest cutoff radius of the MD potential. The one-to-one correspondence between atoms and nodes in the HS region does not break during a dynamic simulation: an atomic trajectory can be viewed as a displacement around the ideal lattice position, and conversely, a nodal displacement can be viewed as a trajectory around the grid point. For this correspondence to be valid, atoms should move around their equilibrium sites without diffusing, and local deformations should be small in order for linear elasticity to hold. For these reasons, the handshake region must be kept far from regions of large deformations, such as the region around a crack tip. A complete MD-HS-FE system for Si(111) is shown in Fig. 3.

The next step is to define the dynamics that the hybrid particles in the HS region will follow. It has been shown by Abraham *et al.*[39] and Rudd and Broughton[40] that it is important to define a single conservative Hamiltonian for the entire system. This ensures that the same symplectic time integrator can be used throughout the MD-HS-FE system, achieving energy conservation and numerical stability throughout the
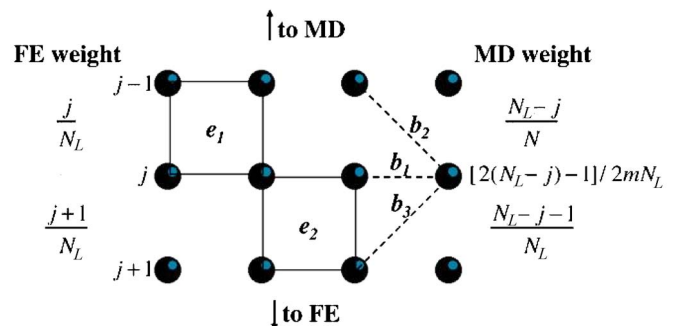

FIG. 4. (Color online) The averaging scheme for the hybrid Hamiltonian.

TABLE I. Average relative weights of the MD and FE interaction terms inside HS.

Relative weight of	MD	FE
between layers $j-1$ and j	$\dfrac{N_L-j}{N_L}$	$\dfrac{j}{N_L}$
within layer j	$\dfrac{2(N_L-j)-1}{2N_L}$	$\dfrac{2j+1}{2N_L}$
between layers j and $j+1$	$\dfrac{N_L-j-1}{N_L}$	$\dfrac{j+1}{N_L}$

FIG. 5. (Color online) Space and task decomposition of the hybrid atomistics-continuum system for parallel computing.

simulation. The kinetic part of the Hamiltonian is handled straightforwardly: within the "lumped mass" approximation, each FE node is assigned a unique mass, which converges to the actual atomic mass within the HS region. The potential part, on the other hand, requires careful treatment: the hybrid particles in the HS region being both atoms and nodes, have both atomistic and/or continuum interaction terms. We thus construct the potential part of the Hamiltonian for the HS region by appropriately averaging the corresponding MD and FE contributions to each hybrid particle.

We develop an improved averaging procedure which is depicted in Fig. 4. As noted earlier, the width of the HS region is set by the longest MD potential cutoff: assume this is equal to N_L atomic layers. Then N_L-1 layers of elements (like e_1 and e_2 in Fig. 4) will fit in the HS and thus contribute by a fractional weight to the Hamiltonian. These weights are shown in the left column of Fig. 4 and correspond to a linear variation with depth in the HS region. For the MD contribution, we assign to each atomic layer j a weight $w_j = [2(N_L-j)-1]/2mN_L$, where $m=2$ or 3 depending on whether we are calculating a two- or three-body MD contribution. Then a two-body interaction between atomic layers j and $j+1$ (e.g., b_3) will contribute to the Hamiltonian a weighting factor of $w_j+w_{j+1}=(N_L-j-1)/N_L$, while b_1 which is within atomic layer j will contribute a weight of $2w_j = [2(N_L-j)-1]/2N_L$. Within the atomic layer j, on the other hand, the FE contribution is given by the average $[j/N_L+(j+1)/N_L]/2$. In a similar manner we treat the three-body MD interactions. For terms between atomic layers j and $j+1$ we have two possibilities: two atoms in layer j and one in layer $j+1$, or one atom in layer j and two in layer $j+1$. If we average these two we also get a weight of $(N_L-j-1)/N_L$. Finally, if any of the atoms of the two- or three-body term is outside the HS, then that term gets a full weight of 1 if that atom is in the MD region or zero weight if it is in the FE region. These weights are summarized in Table I. For our case of Si(111) the Stillinger-Weber potential that we use has only nearest-neighbor terms, and thus only two atomic bilayers (i.e., four atomic layers) are needed inside the HS. Then the average relative weights within bilayer 1 are (3MD+FE)/4, between bilayers 1 and 2 they are (MD+FE)/2, and within bilayer 2 they are (MD+3FE)/4 (we give the same "flavor" to both atomic layers within the bilayer).

This scheme provides a smooth transition from a full MD to a full FE description and it was formulated so as to yield the best mat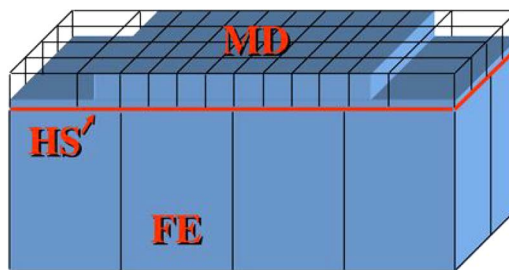ching of the HS elastic constants with those for the pure MD and FE systems. We can now write the total Hamiltonian of our system,

$$H = \frac{1}{2}\sum_i^N m_i v_i^2 + \frac{1}{2}\sum_{i,j}^N (w_i+w_j)V_{ij}^{(2)}(\vec{r}_{ij}) + \frac{1}{6}\sum_{i,j,k}^N (w_i+w_j$$
$$+ w_k)V_{ijk}^{(3)}(\vec{r}_{ij},\vec{r}_{ik}) + \frac{1}{2}\sum_l^{N_{elements}}\sum_{i,j}^{n(l)} w_l \vec{u}_i^l \overset{\leftrightarrow}{k}_{ij}^l \vec{u}_j, \tag{8}$$

where N, $N_{elements}$, and $n(l)$ are the number of total particles, elements, and nodes in element l, respectively. m_i corresponds to particle masses (atoms or nodes are not distinct), $V_{ij}^{(2)}$ and $V_{ijk}^{(3)}$ are the two- and three-body potential terms used in MD, and $\vec{u}^l, \overset{\leftrightarrow}{k}^l$ are the FE displacement vector and stiffness matrix, respectively, for element l.

D. Implementation of multiscale method on parallel computers

Parallel computing requires decomposition of the computation into subtasks and mapping them onto multiple processors. For FE-MD simulations, a divide-and-conquer strategy based on both spatial and task decomposition can be used. The total volume of the MD system is divided into P_{MD} subsystems of equal volume while the total volume of the FE system is divided into P_{FE} subsystems of equal volume, as depicted in Fig. 5. Each subsystem is assigned to a processor in an array of P processors, where $P=P_{MD}+P_{FE}$, and the data associated with particles of a subsystem are assigned to the corresponding processor. The data associated with hybrid atom-node particles of the HS are assigned to the MD processors, while the information about the elements in the HS are kept in the FE processors.

In order to calculate the force on a particle in a subsystem, the coordinates of the particles in the boundaries of neighbor subsystems of the same kind (MD or FE) must be "cached" from the corresponding processors, as well as the coordinates of the hybrid particles from the MD processors to the corresponding FE processors. The calculated forces on the cached particles are subsequently returned to the appropriate processors. After updating the particle positions due to a time-stepping procedure, some particles may have moved out of its subsystem. These particles are "migrated" to the proper neighbor processors. With the spatial decomposition, the computation scales as N/P while communication scales as $(N/P)^{2/3}$ for an N-particle system. The communication over-
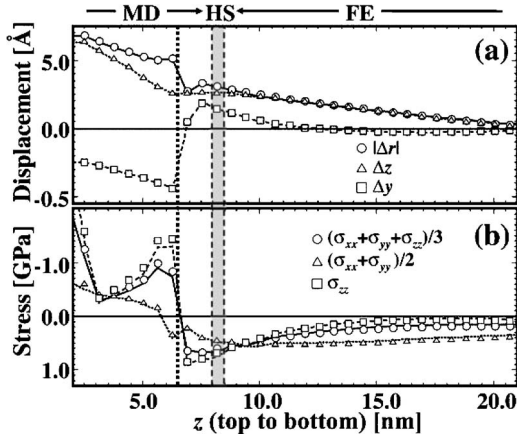
FIG. 6. Excellent agreement between the full MD (symbols) and the hybrid FE-MD (lines) schemes is found: (a) Displacements from equilibrium and (b) stresses as a function of the depth (along z) from the top of the nanopixel. The directions denoted here are x:$[\bar{2}11]$; y:$[0\bar{1}1]$; z:$[111]$. Displacements and stresses are plotted on a vertical line that passes through $x=0$, $y=d/4$, and $x=0$, $y=0$ respectively, where $d=25$ nm is the pixel width and its center is at $x=y=0$. The handshake region (dashed lines) is about 1 nm below the top of the Si substrate, or, about 2 nm below the Si/Si$_3$N$_4$ interface (dotted line).

head thus becomes less significant when N (typically 10^6–10^9 is much larger than $P(10^2$–$10^3)$, i.e., for coarse-grained applications. This scheme is also suitable for meta-computing applications, i.e., when the MD and FE subsystems are assigned to two different (geographically separate) processor arrays.

E. Testing and validation of multiscale method

There are two issues in evaluating the quality of the FE-MD handshake: (i) static agreement, and (ii) dynamic coupling. Static agreement means that a fixed deformation in the MD region will create long-range strain and stress fields that unavoidably extend through the HS into the FE region. A good FE-MD handshake will not alter the values of these fields either inside the HS region or in the FE region from what they would be, had the system been modeled with full MD. In dynamic coupling, on the other hand, we deal with time-dependent deformations, such as displacement or stress waves. A temporal deformation initiated in the MD region, will ultimately propagate through the HS into the FE region. A good FE-MD handshake will not cause artificial reflections of these waves at the HS. If both criteria are satisfied, then the scheme has achieved a seamless coupling between the atomistic and continuum systems.

Testing the static quality of the FE-MD handshake is done on a smaller version of the system that we will study later: a Si/Si$_3$N$_4$ nanopixel. We simulate a $25\times25\times1$-nm Si(111) mesa, covered with a $25\times25\times5$-nm Si$_3$N$_4$ film, on a $50\times50\times15$-nm Si(111) substrate. The Si$_3$N$_4$ film and the Si/Si$_3$N$_4$ interface are treated atomistically with MD while most of the Si substrate is modeled by FE as a continuum. The results of this hybrid simulation are compared with those
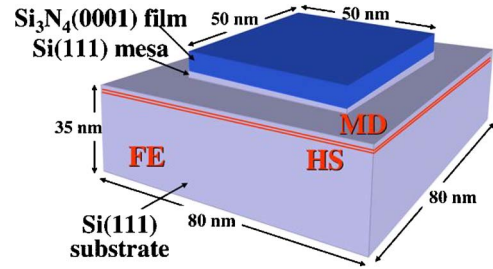

FIG. 7. (Color online) The simulated Si/Si$_3$N$_4$ nanopixel.

obtained by using a full MD description of an identical system. Periodic boundary conditions are applied on the sides of the substrate, while its bottom is held fixed. We simulate both crystalline (0001) and amorphous Si$_3$N$_4$ films. In the case of the crystalline film, the interface remains coherent and so the resulting stress fields are uniform (parabolic stress well). In the case of an amorphous film, the interface is incoherent and the stress fields are nonuniform (stress domains). The origin and the dynamics of these stress patterns will be the focus of the next section.

For the crystalline Si$_3$N$_4$ case, the comparison between displacement fields of the full MD and the hybrid FE-MD simulations is summarized in Fig. 6. The HS region in the hybrid simulation is only 1 nm below the top of the Si substrate and 2 nm below the Si/Si$_3$N$_4$ interface. The displacements from equilibrium as a function of the depth z from the top of the pixel are plotted in Fig. 6(a) with symbols and lines for the MD and hybrid systems, respectively. Of similar quality is the agreement between the local stress distributions in the full MD and hybrid FE-MD schemes, shown in Fig. 6(b). To study the effect of the position of the HS region, we perform another FE-MD simulation where the HS is placed 3 nm below the top of the Si substrate instead of 1 nm. Results with two different HS positions are practically identical. This justifies the use of a HS region close to the interface resulting in a highly cost-effective hybrid FE-MD system.

In a second simulation we studied the quality of the dynamic coupling between MD and FE. The system here consists of a block of silicon, one-third of it modeled with MD and the remaining two-thirds modeled by FE, and the simulation involves a projectile impact. The silicon block has dimensions of $11\times6\times30$ nm^3 with the HS parallel to the (111) plane 10 nm below the top Si surface. Periodic boundary conditions are imposed on the sides. The top Si surface in the MD region is free and the nodes at the bottom Si surface in the FE region are fixed. The projectile impact at the top Si surface in the MD region created small-amplitude waves in the silicon crystal that propagated through the HS into the FE region without reflection, demonstrating seamless dynamic handshaking between MD and FE.

IV. STRAIN RELAXATION DYNAMICS IN Si/Si$_3$N$_4$ NANOPIXELS

Here we apply our multiscale MD-FE simulation approach to investigate possible strain relaxation mechanisms in Si/Si$_3$N$_4$ nanopixels. This system has been shown to grow
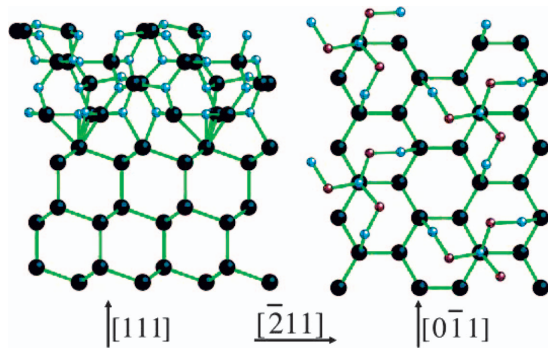
FIG. 8. (Color) Two different projections of the Si(111)/Si$_3$N$_4$(0001) interface. Silicon atoms are shown in black and nitrogen atoms in blue. In the (111) projection (right plot) we show the silicon atoms of the Si$_3$N$_4$ film in brown and plot only the two atomic layers across the interface for clarity of presentation.

with a 2D growth mode.[31,42,43] Therefore we will assume a flat Si$_3$N$_4$ film of a fixed thickness. The simulated system is depicted in Fig. 7. A 50×50-nm^2 and 8-nm-thick Si$_3$N$_4$ film resides on a 50×50-nm^2 and 1-nm-thick Si(111) mesa, which in turn sits on a larger 80×80-nm^2 and 35-nm-thick Si(111) substrate. A simple application of the classical Matthews and Blakeslee formula for the critical thickness gives an estimate of $h_c \sim 2$ nm. The edges of the Si mesa are free to relax laterally, thus providing the beneficial effects of a compliant substrate. At the sides of the Si substrate we apply periodic boundary conditions while its bottom is held fixed. Two different structures of the Si$_3$N$_4$ film are studied—a crystalline α-phase Si$_3$N$_4$(0001) structure as well as an amorphous Si$_3$N$_4$ structure. Within our multiscale simulation implementation, the Si$_3$N$_4$ film, the Si mesa, and the top 1 nm portion of the Si substrate, which includes the free surface, are modeled with MD, while the remaining part of the substrate is modeled with the FE method. The handshake region is thus just 2 nm below the Si/Si$_3$N$_4$ interface.

The lattice constant of Si$_3$N$_4$ is larger than that of Si by 1.25%. We start the simulation with a scaled SW potential that produces a larger lattice constant for the Si mesa and substrate by 1.25%, thus initializing an unstrained pseudo-
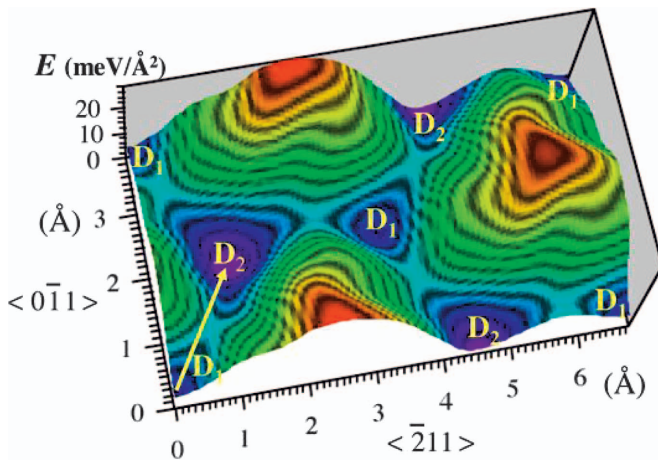

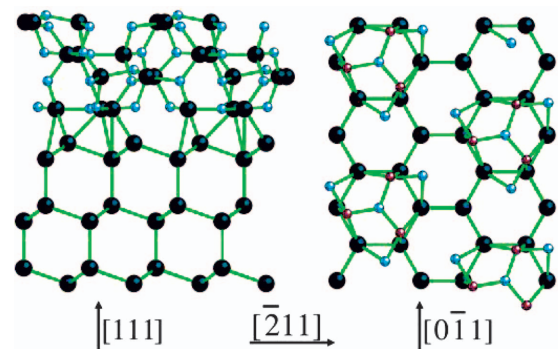FIG. 9. (Color) Stacking fault energy diagram for the Si/Si$_3$N$_4$ interface.

FIG. 10. (Color) Two different projections of the D$_2$ Si(111)/Si$_3$N$_4$(0001) interface structure.

Si/Si$_3$N$_4$ system. The system is slowly brought to equilibrium at 300 K in 24 ps. Temperature is controlled using Langevin dynamics throughout the whole system (MD, HS, and FE). The mismatch is introduced in the next 24 ps by gradually scaling the SW potential back to its original parameters while maintaining the temperature at 300 K. We subsequently remove the temperature control and let the system relax for an additional 24 ps, after which we quench the system back to zero temperature. During this process we monitor the interface structure and follow the strain relaxation dynamics. In all cases, the interface structure is found to be stable at the end of the simulation.

In the following, we study the atomic structure, the symmetries and the energetics of the Si(111)/Si$_3$N$_4$(0001) interface. We then present our simulation results for the Si(111)/Si$_3$N$_4$(0001) system shown in Fig. 7. Finally we present results obtained by varying the temperature, the compliant Si mesa, as well as the structure of the Si$_3$N$_4$ film.

A. Coherent Si(111)/Si$_3$N$_4$(0001) interface structure

The structure of a coherent Si(111)/Si$_3$N$_4$(0001) interface is shown at two different projections in Fig. 8, which is a
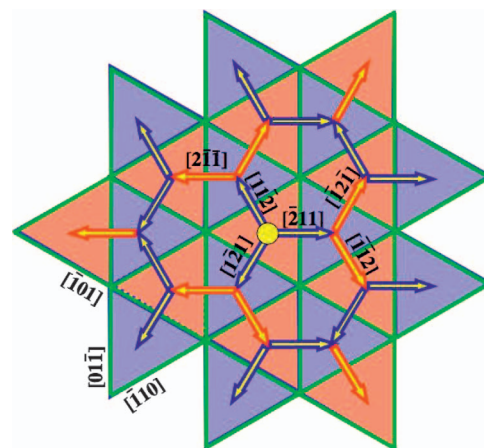

FIG. 11. (Color) The proposed interface structure for the relaxed Si/Si$_3$N$_4$ interface. Here the initial coherent interface is assumed to be a "red" state, which is denoted by the yellow dot in the middle triangle.

local energy minimum configuration obtained by LCAO calculations.[70] The important interfacial bonding is between the unsaturated nitrogen and silicon atoms in the bottom Si_3N_4 and top Si layers, respectively, at a bond length of 1.75 Å. The Si—Si neighbor distance across the interface is around 2.7 Å. If the two layers are at infinite separation, the total surface energy is 486 meV/Å^2; when the surfaces are brought together, it is 430 meV/Å^2. We can thus estimate an "interface energy" of $E_{INT} = -56$ meV/Å^2.

Important information about the energetics of strain relaxation can be obtained by plotting the energy change due to a relative slip across the interface between Si and Si_3N_4, i.e., the stacking fault energy diagram (in practice in this unit-cell calculation the two parts of the interface just slide with respect to each other). A unit cell of the interface in the $\langle \bar{2}11 \rangle$ and $\langle 0\bar{1}1 \rangle$ directions (denoted as the x and y directions, respectively, in what follows) is used, and 5 unit cells for each of Si and Si_3N_4 in the $\langle 111 \rangle$ direction (denoted as the z direction). In order to have a coherent interface, the Si lattice is expanded by 1.25% to match the Si_3N_4 lattice constant (without scaling the SW potential). Periodic boundary conditions are applied in the x and y directions, while both surfaces in the z direction are let free to relax (atoms are allowed to relax only in the z direction, i.e., possible surface reconstructions are not taken into account). The convergence of the results is confirmed by increasing the number of cells in the z direction. Figure 9 shows the stacking-fault energy for relative slips of the Si/Si_3N_4 interface along the x and y directions. The zero-slip case, which corresponds to the interface structure of Fig. 8, is denoted by D_1. We note that there is a second local energy minimum interface structure, at the relative slip denoted by D_2. The arrow denoting a $D_1 \rightarrow D_2$ slip lays along the $[\bar{1}2\bar{1}]$ direction and is $b = c_x \hat{x}/6 + c_y \hat{y}/2$, where c_x and c_y are the two lateral lattice constants of the Si(111) orthorhombic unit cell. Using the strain-relaxed, zero-temperature values $c_x = 6.6515$ Å and $c_y = 3.8403$ Å we find $|b| = 2.2172$ Å. The interface structure D_2 is actually lower in energy than D_1 by ~3 meV/Å^2, and they are separated by an energy barrier of ~10 meV/Å^2. This is considerably lower than the energy barrier encountered during a $D_1 \rightarrow D_1$ slip (~25 meV/Å^2). The $D_1 \rightarrow D_2$ and $D_2 \rightarrow D_1$ slips are thus expected to be the dominant modes of strain relaxation in this system.

In Fig. 10 we plot the same two projections as in Fig. 8 of the interface structure at D_2. Each nitrogen atom in the bottom layer of the Si_3N_4 film has three silicon atoms as neighbors across the interface at an enlarged separation distance of about 2.5 Å. At the same time, the silicon atoms in the bottom layer of the Si_3N_4 film are neighbors of one silicon atom across the interface at a separation distance of 2.4 Å, which is ~1.25% larger than the Si—Si bond length in diamond silicon. In the rest of this work, we will use the number of Si neighbors to each nitrogen atom across the interface to determine the interface structure.

Assuming that successive $D_1 \rightarrow D_2$ and $D_2 \rightarrow D_1$ slips relax the mismatch strain, we show the resulting interface structure in Fig. 11: It is a triangular superlattice of interfacial domains D_1 and D_2. Blue color denotes D_1 state, and red D_2. The red and blue arrows denote $D_1 \rightarrow D_2$ and $D_2 \rightarrow D_1$
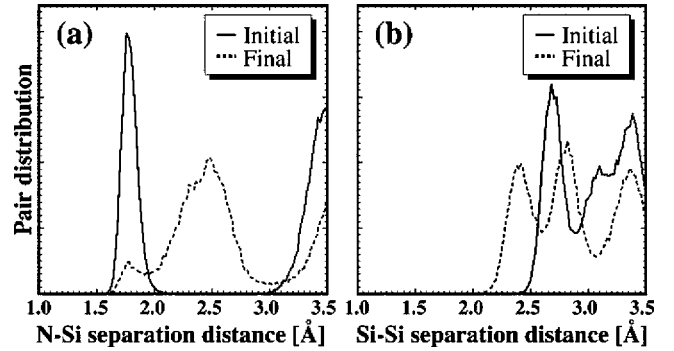

FIG. 12. (a) N—Si and (b) Si—Si distance distribution across the interface, before (initial) and after (final) the strain relaxation.

slips, respectively, along the $\langle \bar{2}11 \rangle$ directions, while the green lines denote the corresponding interfacial domain boundaries, which are along the $\langle 0\bar{1}1 \rangle$ symmetry directions. These interfacial domain boundaries are reminiscent of misfit dislocations, and thus we expect them to have similar properties.

The interfacial domain boundary structure of Fig. 11 is the equivalent of a complete network of partial dislocations, lying along the $\langle 0\bar{1}1 \rangle$ directions and arranged in a triangular lattice. This is different from a network of full dislocations that would lie along the $\langle \bar{2}11 \rangle$ directions, with their Burgers vector along the $\langle 0\bar{1}1 \rangle$ directions and arranged into a honeycomb lattice. Such a case has been observed[17] and studied[18] for the InAs/GaAs(111) interface. In that system, strain is relaxed predominantly through $D_1 \rightarrow D_1$ slips. However, it is found that at every other vertex of the honeycomb lattice, where three dislocation lines meet, the strain becomes excessive, forcing the full dislocations to split into partials, forming a small triangular region around the vertex.

B. Strain relaxation in the Si(111)/Si_3N_4(0001) interface

We followed the simulation schedule described at the beginning of this section for the system depicted in Fig. 7. During the simulation we monitor the interface structure, i.e., the instantaneous separation between nitrogen and silicon atoms across the interface as well as the average number of substrate silicon atoms that are close neighbors of nitrogen atoms in the film. We find that the interface remains coherent in the presence of the mismatch and temperature control (Langevin) until the end of the second part of the simulation (at 48 ps). This is because the Langevin dynamics suppresses coherent motion and thus the relaxation of the interface. Large compressive and tensile stresses (>1 GPa) appear in the film and substrate, respectively, due to the mismatch. It is not until the third part of the simulation, where we remove the temperature control, that the strain relaxation mechanisms become operative. The N—Si and Si—Si separation distance distribution across the interface is plotted in Fig. 12 at two time instances, just before we release the temperature control (48 ps) and just before we start quenching the system back to zero temperature (72 ps). We note that the entire
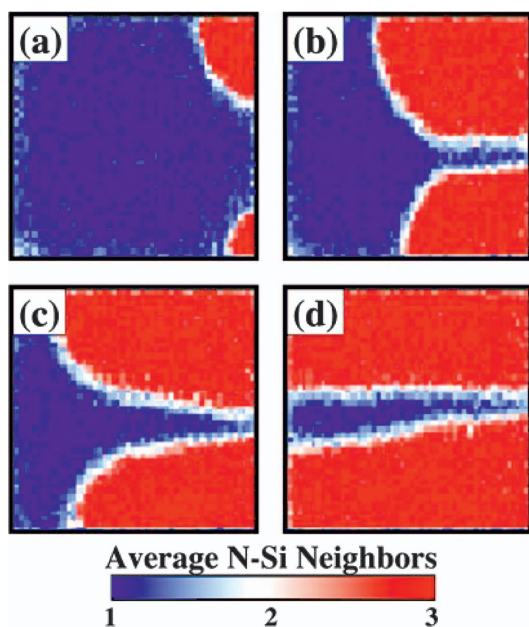
Average N-Si Neighbors

1   2   3

FIG. 13. (Color) Dynamics of strain relaxation: interface structure at (a) 6 ps, (b) 12 ps, (c) 18 ps, and (d) 24 ps after the temperature control is removed and strain relaxation initiates. Blue color denotes D_1 interface state and red denotes D_2. White corresponds to the interfacial domain boundaries.

Vertical position [Å]

0.0   0.5   1.0   0.5   2.0

FIG. 15. (Color) Vertical interface modulation at (a) 6 ps, (b) 12 ps, (c) 18 ps, and (d) 24 ps. Deep modulations correspond to the interfacial domain boundaries. The vertical length scale is magnified by a factor of 100 and truncated at 2.0 Å for better visualization.

interface, except for a small part, has slipped into a D_2 interface configuration.

In order to understand the dynamic evolution of this transition, we color code in Fig. 13 the average number of substrate silicon atoms that are close neighbors of nitrogen atoms in the film, or the "average number of N—Si neighbors" across the interface, at four time instances: 6, 12, 18, and 24 ps after the temperature control was removed. Averaging was done in voxels of size 1×1 nm^2. We note that the new interfacial domains nucleate at the free corners

(highest energy points) and the corresponding interfacial domain boundaries move inwards through successive slips at an estimated speed of $\sim 2.5 \pm 0.5$ km/s. For comparison, the Rayleigh speeds in Si and Si$_3$N$_4$ are about 3.25 and 6.4 km/s, respectively. In the final frame, two nearly parallel interfacial domain boundaries along the $[\bar{2}11]$ direction are settled in the middle of the interface, separated by a narrow D_1 interface domain. The width of this narrow domain is determined by the balance of two forces: one forcing the D_2 domain to expand since it is lower in energy than D_1, and another forcing the two domain boundaries apart from each
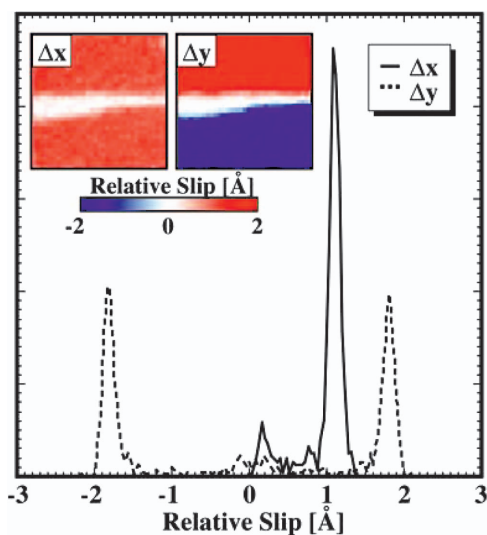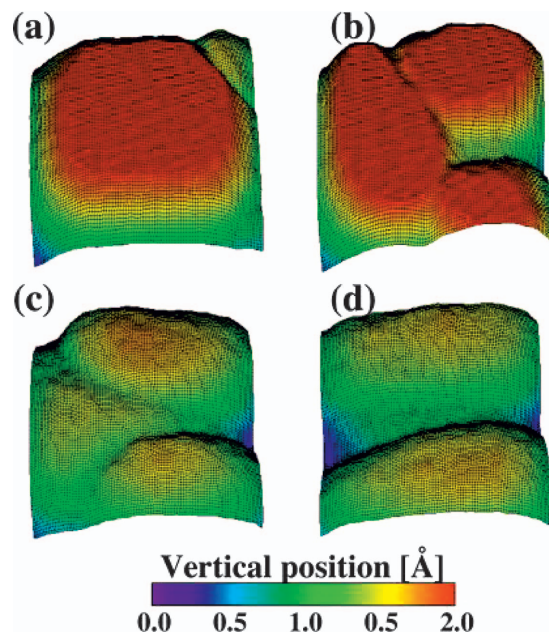

FIG. 14. (Color) Relative slip between the film and substrate. The two inset graphs have the x and y components of the slip color-coded throughout the interface.

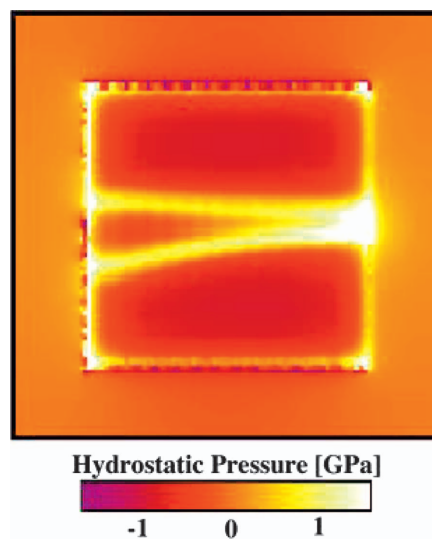**Hydrostatic Pressure [GPa]**

-1   0   1

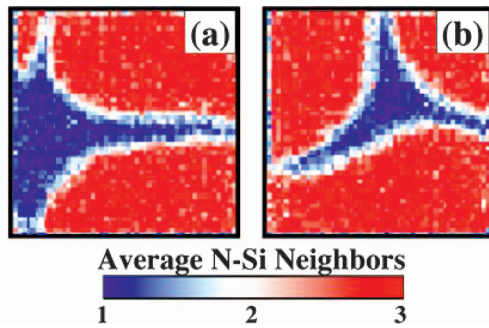FIG. 16. (Color) Residual stresses on a plane just below the top of the silicon substrate.

FIG. 17. (Color) Average N—Si neighbors for the system in Fig. 7 at a temperature of $T=600$ K. Frame (b) is taken 15 ps after frame (a).

FIG. 19. (Color) Interface configuration for the amorphous Si_3N_4 film case. First and second rows are at 1 and 10 ps, respectively, after we start introducing the mismatch in the second part of the simulation schedule, while the third row is at the end of the simulation. First (second) column corresponds to an initial interface prepared in a D_1 (D_2) configuration. Yellow lines mark the corresponding domain boundaries.

other in order to maximize the strain relaxation effect. We further note that the domain boundary line is not along the expected lines from Fig. 11. The reason for this discrepancy is that the actual length scale of the relaxed interface has not been reached, i.e., this is an artifact of the finite size of the pixel. As we will later see, when we change the initial conditions in order to induce more domains (and thus more domain boundaries), this is no longer the case.

In order to verify the slip directions and magnitudes proposed earlier, we plot in Fig. 14 the distribution of relative slips between film and substrate. In the two inset figures we color-code the relative slips in the x and y directions. The upper part has slipped by $b_1=\hat{x}c_x/6+\hat{y}c_y/2$ while the lower part has slipped by $b_2=\hat{x}c_x/6-\hat{y}c_y/2$. The third possible slip $b_3=-\hat{x}c_x/3$ did not become operative. The angle between the slip vector and the domain boundary line is 60°, which in dislocation terminology corresponds to 3/4 edge and 1/4 screw flavors.

When an elastic solid is biaxially compressed, it expands along the third dimension due to the Poisson effect. In our case of a finite-size film, it also bends to partially relieve some of the applied strain. When interfacial domain boundaries are present, the strain is released, or even reversed locally, thereby introducing a corresponding modulation of the interface and film morphology. Such modulations are characteristic of misfit dislocations and have been studied by STM measurements in semiconductor heteroepitaxial systems.[16,17] Figure 15 shows the interface's vertical modu-

lation at the same four time instances as in Fig. 13. The maximum vertical displacement in (a) and (b) reaches 2.7 Å, but it is truncated for better visualization. We note that the interface modulation closely follows the domain boundaries. At the end of the simulation, the maximum vertical displacement is significantly smaller than its initial value, indicating substantial strain relief. This demonstrates the beneficial role of the domain boundaries in strain relaxation.

After the system is quenched down to zero temperature, the remaining issue is the nature of residual stresses. In Fig. 16 we plot the hydrostatic pressure on a plane parallel to the interface just below the top of the silicon substrate. We see
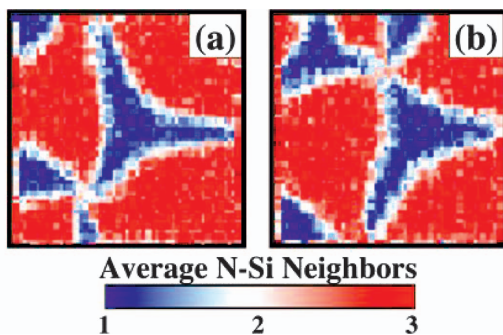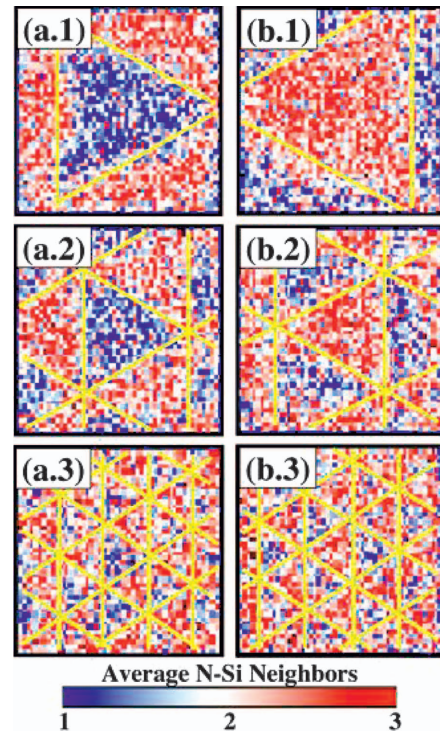

FIG. 18. (Color) Average N—Si neighbors for the system in Fig. 7 at a temperature of $T=600$ K for two different initial conditions: (a) a coherent D_1 interface and (b) a coherent D_2 interface. The scale of the domains formed is the same in both cases.
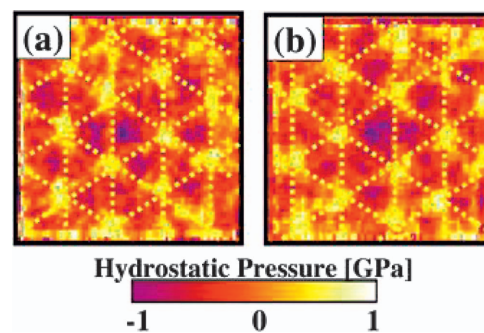

FIG. 20. (Color) Residual stresses for the relaxed systems shown in Figs. 19(a.3) and 19(b.3).

that high compressive stresses appear directly below the domain boundaries, while stresses remain tensile below the coherent parts of the interface. There is no difference between the stresses below the D_1 or D_2 interface region. The effect of the strain relaxation is also seen in part of the substrate around the pixel: along the y direction the residual stresses have diminished, while along the x direction they remain compressive. It is worth noting that our test simulation on the 25×25 nm^2 system, as well as previous simulations on a 34×53 nm^2 system,[31] did not reveal any strain relaxation mechanism, i.e., the interface remained coherent throughout the simulation. The current system size is just enough to force the coherent-to-semicoherent interface transition, and therefore a larger system size or different initial conditions are needed to probe further relaxation. The latter is the subject of the next section.

C. Controlling the domain size in the Si/Si$_3$N$_4$ interface

Nucleation of new interfacial domains and domain boundary propagation rates depend on the energetics of the particular problem. For example, for a given film thickness, the larger the lateral size of the interface, the larger the mismatch strain energy that drives the formation of new interfacial domains. For a given system size we may control the strain relaxation mechanisms, and thus the interface domain structure, by directly controlling the energetics of the domain boundaries. Three different approaches are discussed below: temperature, compliance, and film structure.

In Fig. 17 we plot the interface structure at two time instances for the same system as before but at a higher temperature $T = 600$ K. We expect that the elevated temperature will provide the additional energy required for the nucleation of more interfacial domains. Indeed, while the domain boundary motion initially proceeds similarly to the $T = 300$ K case [initial stages are exactly as in Figs. 13(a) and 13(b)], a third interfacial domain boundary appears just before the other two reach the interface edge, forcing them back to the center. The domain boundary lines are now closer to those in Fig. 11.

The next approach deals with the thin compliant Si(111) layer between the film and the substrate. Compliant substrates are an important subject of current research because they are able to accommodate much of the mismatch strain. In our case, it provides the lateral space for the film to partially relax,[49] thus lowering the total mismatch strain energy and suppressing the strain relaxation process. Removing the thin Si(111) compliant layer will increase the mismatch strain energy and thus enhance the strain relaxation processes, i.e., it will increase the number of interfacial domains in the interface. We performed this simulation at a temperature of $T = 600$ K for two different initial conditions: (a) a coherent D_1 interface, and (b) a coherent D_2 interface. Results are shown in Fig. 18. Both initial conditions yield the same result: more domains are formed and the corresponding domain boundaries lie closer to those of Fig. 11. On the average, there is more coverage by the D_2 interfacial state, which is expected since it is slightly lower in energy than D_1. This is also the reason why the domain boundary lines are

not straight but rather curved. As mentioned earlier, it is the balance of two forces that determine the interfacial domain boundary structure: one forcing the maximum D_2 interface coverage, and the other forcing the domain boundaries in a spread configuration. Comparing with the previous results, however, the latter force seems to be dominant: the mismatch strain energy to be relieved is much greater when the compliant layer is removed. These results demonstrate the beneficial role of a thin compliant layer between the film and the substrate in suppressing or delaying the coherent-to-semicoherent interface transition.

Our final approach is concerned with the structure of the Si$_3$N$_4$ film. In particular, we consider the amorphous a-Si$_3$N$_4$ film, which was prepared from a c-Si$_3$N$_4$(0001) block by heating it to 6000 K and subsequently cooling it, while keeping the atoms in the bottom monolayer fixed at their crystalline positions. This ensures that the lattice mismatch of 1.25% between Si(111) and c-Si$_3$N$_4$(0001) as well as the coherency at the interface are retained in our simulation. The energetics of interfacial domain nucleation and domain boundary propagation, however, change. The stacking fault energy diagram of Fig. 9 and the corresponding energy barriers are substantially flatter, easing the generation and propagation of domain boundaries. The energy difference between D_1 and D_2 is also much smaller. Given these conditions, we expect the interface structure to be much closer to the relaxed interface structure of Fig. 11. The Si(111) mesa and substrate remain the same as before, while the simulation temperature is $T = 300$ K.

Figure 19 shows our simulation results for the amorphous film. The first (second) column corresponds to a system initialized in a coherent D_1 (D_2) interface configuration. The yellow lines mark the corresponding domain boundaries for clarity of presentation, since there is much more noise in the case of an amorphous film than in the crystalline film. The first two rows of frames are taken at two time instances in the second part of the simulation, 1 and 10 ps after introducing the mismatch. We note that interfacial domain nucleation and domain boundary propagation occur even though the temperature control is still on. This is an indication of a flatter stacking fault energy surface, and thus easier for domain boundary nucleation and propagation, as mentioned earlier. The third row of frames is at the end of the third part of the simulation, where the whole structure is fully relaxed.

The interfacial domain boundaries are indeed arranged in a perfect triangular network lying along the Si $\langle 0\bar{1}1 \rangle$ symmetry directions with the corresponding slips along the Si $\langle \bar{2}11 \rangle$ symmetry directions. In dislocation terminology, these domain boundaries are of edge type. As the lattice mismatch is gradually introduced, new interfacial domains nucleate at the free edges and corners of the interface and the corresponding domain boundaries move inwards without ever diverting from the triangular arrangement. We also note that there is no significant difference in area coverage between interface structure D_1 and D_2, indicating that their energy difference is now insignificant.

The residual stresses in the Si substrate just below the interface, shown in Fig. 20, consist of a uniform tensile background on top of which there is a triangular lattice of com-

pressive stress domains. These domains are just below the vertices of the interfacial domain boundary network, where three domain boundaries meet resulting in highly compressive stresses. Along the domain boundaries we also see small compressive stresses. Within each interface domain there are uniform tensile stresses, indicating that the interface above them is still coherently matched. Overall, however, these stress values are smaller than the corresponding stresses in the case of a crystalline film. The size of these domains is in accordance with the simple estimate $L \sim |b|/\varepsilon_m = 17.75$ nm leading to the conclusion that the mismatch strain in this case is fully relaxed. By using a film of graded structure, we should be able to achieve any intermediate degree of relaxation and thus fully control the interfacial structure.

V. CONCLUSIONS

We have used a multiscale simulation approach to gain physical insight into the strain relaxation mechanisms in Si/Si_3N_4 nanopixels. Our findings may be summarized as follows:

(i) A possible mechanism for strain relaxation involves the formation of a network of interfacial domain boundaries. These are the equivalent of interfacial partial misfit dislocations, as they have the same symmetries and strain relief properties.

(ii) These domain boundaries appear due the nucleation of interfacial domains at the edges and corners of the mesa structure, and subsequently propagate inwards. A rough estimate of the propagation speed is ~ 2.5 km/s. The effect of temperature is to increase the nucleation rate.

(iii) The equilibrium shape and arrangement of the domain boundary network is determined by the balance of two opposing forces, one trying to minimize the interfacial bond-

ing energy and another trying to maximize the strain energy being released.

(iv) The existence of a thin compliant Si layer between the film and the substrate provides the necessary lateral space for partial strain relaxation, thus suppressing the interfacial domain nucleation rate.

(v) Changing the structure of the film changes the energy terrain for the domain boundaries and thus their equilibrium configuration. In the amorphous film, strain is fully relaxed by a complete network of perfect partial domain boundaries, arranged in a perfect triangular lattice.

(vi) High residual stresses appear along the domain boundary lines and especially at the vertices where two or more lines meet.

The multiscale simulation approach has proven to be an excellent tool for the study of strain relaxation mechanisms in strained heteroepitaxial systems. By using the appropriate methodology for each part of the system, we were able to follow complex atomistic processes at finite temperature within systems of realistic sizes and shapes. Here we have combined the predictive power of an atomistic approach with the large length scale accessibility of a continuum method, necessary for direct comparison and interpretation of experimental data. This methodology is expected to prove very useful in future applications on similar multiscale problems such as strain relaxation in other heteroepitaxial systems, nanoindentation of thin films, high-speed impact on thin film coatings, etc.

[1] See, e.g., articles in *Heteroepitaxy and Strain: Applications to Electronic and Optoelectronic Materials*, edited by L. J. Schowalter, Mater. Res. Bull., 21, 4 (1993), and references therein.

[2] J. H. Van der Merwe, J. Appl. Phys. **34**, 123 (1962).

[3] J. W. Matthews and A. E. Blakeslee, J. Cryst. Growth **27**, 118 (1974).

[4] J. C. Bean, L. C. Feldman, A. T. Fiory, S. Nakahara, and I. K. Robinson, J. Vac. Sci. Technol. A **2**, 436 (1984).

[5] R. People and J. C. Bean, Appl. Phys. Lett. **47**, 322 (1985).

[6] J. Y. Tsao, B. W. Dodson, S. T. Picraux, and D. M. Cornelison, Phys. Rev. Lett. **59**, 2455 (1987).

[7] L. B. Freund and W. D. Nix, Appl. Phys. Lett. **69**, 173 (1996).

[8] J. P. Hirth and X. Feng, J. Appl. Phys. **67**, 3343 (1990); X. Feng and J. P. Hirth, *ibid.* **72**, 1386 (1992).

[9] F. Y. Huang, Phys. Rev. Lett. **85**, 784 (2000).

[10] A. Ohtake and M. Ozeki, Phys. Rev. Lett. **84**, 4665 (2000).

[11] A. Madhukar, J. Cryst. Growth **163**, 149 (1996).

[12] B. J. Spencer, P. W. Voorhees, and S. H. Davis, Phys. Rev. Lett. **67**, 3696 (1991).

[13] J. Tersoff and R. M. Tromp, Phys. Rev. Lett. **70**, 2782 (1993).

[14] B. J. Spencer and J. Tersoff, Phys. Rev. Lett. **79**, 4858 (1997).

[15] E. Y. Lee, S. Bhargava, M. A. Chin, V. Narayanamurti, K. J. Pond, and K. Luo, Appl. Phys. Lett. **69**, 940 (1996).

[16] J. G. Belk, J. L. Sudijono, X. M. Zhang, J. H. Neave, T. S. Jones, and B. A. Joyce, Phys. Rev. Lett. **78**, 475 (1997).

[17] H. Yamaguchi, J. G. Belk, X. M. Zhang, J. L. Sudijono, and M. R. Fahy, Phys. Rev. B **55**, 1337 (1997).

[18] L. A. Zepeda-Ruiz, D. Maroudas, and W. H. Weinberg, J. Appl. Phys. **85**, 3677 (1999).

[19] S. Srinivasan, L. Geng, R. Liu, F. A. Ponce, Y. Narukawa, and S. Tanaka, Appl. Phys. Lett. **83**, 5187 (2003).

[20] S. H. Oh and C. G. Park, J. Appl. Phys. **95**, 4691 (2004).

[21] E. Kuramochi, J. Temmyo, and T. Tamamura, Appl. Phys. Lett. **71**, 1655 (1997).

[22] S. C. Jain, A. H. Harker, A. Atkinson, and K. Pinardi, J. Appl. Phys. **78**, 1630 (1995); S. C. Jain, H. E. Maes, K. Pinardi, and I. De Wolf, *ibid.* **79**, 8145 (1996).

[23] H. T. Johnson and L. B. Freund, J. Appl. Phys. **81**, 6081 (1997).

[24] Y. Zhuang, V. Holý, J. Stangl, A. A. Darhuber, P. Mikulik, S. Zerlauth, F. Schäffler, G. Bauer, N. Darowski, D. Lübbert, U.

Pietsch, J. Phys. D **32**, 224 (1999).

[25] G. S. Pearson and D. A. Faux, J. Appl. Phys. **88**, 730 (2000).

[26] A. C. Schindler, M. F. Gyure, G. D. Simms, D. D. Vvedensky, R. E. Caflisch, C. Connell, and E. Luo, Phys. Rev. B **67**, 075316 (2003).

[27] A. M. Andrews, R. LeSar, M. A. Kerner, J. S. Speck, A. E. Romanov, A. L. Kolesnikova, M. Bobeth, and W. Pompe, J. Appl. Phys. **95**, 6032 (2004).

[28] Z. Zhang and M. G. Lagally, Phys. Rev. Lett. **72**, 693 (1994).

[29] W. Yu and A. Madhukar, Phys. Rev. Lett. **79**, 905 (1997); **79**, 4939(E) (1997).

[30] M. A. Cusack, P. R. Briddon, and M. Jaros, Phys. Rev. B **54**, R2300 (1996).

[31] M. E. Bachlechner, A. Omeltchenko, A. Nakano, R. K. Kalia, P. Vashishta, I. Ebbsjö, A. Madhukar, and P. Messina, Appl. Phys. Lett. **72**, 1969 (1998); A. Omeltchenko, M. E. Bachlechner, A. Nakano, R. K. Kalia, P. Vashishta, I. Ebbsjö, A. Madhukar, and P. Messina, Phys. Rev. Lett. **84**, 318 (2000).

[32] C. Pryor, J. Kim, L. W. Wang, A. J. Williamson, and A. Zunger, J. Appl. Phys. **83**, 2548 (1998).

[33] M. A. Makeev and A. Madhukar, Phys. Rev. Lett. **86**, 5542 (2001).

[34] Y. Kikuchi, H. Sugii, and K. Shintani, J. Appl. Phys. **89**, 1191 (2001).

[35] M. Mullins and M. A. Dokainish, Philos. Mag. A **46**, 771 (1982).

[36] S. Kohlhoff, P. Gumbsch, and H. F. Fischmeister, Philos. Mag. A **64**, 851 (1991).

[37] E. B. Tadmor, M. Ortiz, and R. Phillips, Philos. Mag. A **73**, 1529 (1996); J. Knap and M. Ortiz, J. Mech. Phys. Solids **49**, 1899 (2001).

[38] O. A. Shenderova, D. W. Brenner, A. A. Nazarov, A. E. Romanov, and L. H. Yang, Phys. Rev. B **57**, R3181 (1998).

[39] F. F. Abraham, J. Q. Broughton, N. Bernstein, and E. Kaxiras, Comput. Phys. **12**, 538 (1998).

[40] R. E. Rudd and J. Q. Broughton, Phys. Rev. B **58**, R5893 (1998); Phys. Status Solidi B **217**, 251 (2000).

[41] E. Lidorikis, M. E. Bachlechner, R. K. Kalia, A. Nakano, P. Vashishta, and G. Z. Voyiadjis, Phys. Rev. Lett. **87**, 086104 (2001).

[42] Y. Nakada, I. Aksenov, and H. Okumura, Appl. Phys. Lett. **73**, 827 (1998).

[43] X. Wang, G. Zhai, J. Yang, and N. Cue, Phys. Rev. B **60**, R2146 (1999).

[44] K. Pinardi, U. Jain, S. C. Jain, H. E. Maes, R. Van Overstraeten, and M. Willander, J. Appl. Phys. **83**, 4724 (1998).

[45] B. J. Spencer and J. Tersoff, Appl. Phys. Lett. **77**, 2533 (2000).

[46] D. Maroudas, L. A. Zepeda-Ruiz, and W. H. Weinberg, Appl. Phys. Lett. **73**, 753 (1998).

[47] T. C. Wang, Y. W. Zhang, and S. J. Chua, Acta Mater. **49**, 1599 (2001).

[48] K. Wiesauer and G. Springholz, Appl. Phys. Lett. **83**, 5160 (2003).

[49] S. Luryi and E. Suhir, Appl. Phys. Lett. **49**, 140 (1986).

[50] A. R. Powell, S. S. Iyer, and F. K. LeGoues, Appl. Phys. Lett. **64**, 1856 (1994).

[51] F. E. Ejeckam, Y. H. Lo, S. Subramanian, H. Q. Hou, and B. E. Hammons, Appl. Phys. Lett. **70**, 1685 (1997).

[52] W. A. Jesser, J. H. van der Merwe, and P. M. Stoop, J. Appl. Phys. **85**, 2129 (1999).

[53] Y. Obayashi and K. Shintani, J. Appl. Phys. **88**, 5623 (2000).

[54] T. Y. Tan and U. Gösele, Appl. Phys. A: Mater. Sci. Process. **64A**, 631 (1997); G. Kästner, U. Gösele, and T. Y. Tan, *ibid.* **66A**, 13 (1998); G. Kästner and U. Gösele, J. Appl. Phys. **88**, 4048 (2000).

[55] J. P. Hirth and J. Lothe, *Theory of Dislocations* (Krieger, Malabar, FL, 1982).

[56] K. Pinardi, S. C. Jain, M. Willander, A. Atkinson, H. E. Maes, and R. Van Overstraeten, J. Appl. Phys. **84**, 2507 (1998).

[57] X. T. Su, R. K. Kalia, A. Madhukar, A. Nakano, and P. Vashishta, Appl. Phys. Lett. **78**, 3717 (2001).

[58] A. Konkar, A. Madhukar, and P. Chen, in *Materials—Fabrication and Patterning at the Nanoscale*, edited by C. R. K. Marrian, K. Kash, F. Cerrina, and M. Lagally, Mater. Res. Soc. Symp. Proc. 80 (Materials Research Society, Pittsburgh, 1995), p. 12; Appl. Phys. Lett. **72**, 220 (1998).

[59] B. Z. Nosho, L. A. Zepeda-Ruiz, R. I. Pelzel, W. H. Weinberg, and D. Maroudas, Appl. Phys. Lett. **75**, 829 (1999).

[60] J. Jacobsen, B. H. Cooper, and J. P. Sethna, Phys. Rev. B **58**, 15847 (1998).

[61] V. B. Shenoy, R. Miller, E. B. Tadmor, R. Phillips, and M. Ortiz, Phys. Rev. Lett. **80**, 742 (1988).

[62] E. B. Tadmor, R. Miller, R. Phillips, and M. Ortiz, J. Mater. Res. **14**, 2233 (1999); J. Knap and M. Ortiz, Phys. Rev. Lett. **90**, 226102 (2003).

[63] R. E. Miller and E. B. Tadmor, J. Comput.-Aided Mater. Des. **9**, 203 (2002).

[64] N. M. Ghoniem, E. P. Busso, N. Kioussis, and H. Huang, Philos. Mag. A **83**, 3475 (2003).

[65] D. Moldovan, D. Wolf, and S. R. Phillpot, Philos. Mag. A **83**, 3643 (2003).

[66] J. A. Moriarty, V. Vitek, V. V. Bulatov, and S. Yip, J. Comput.-Aided Mater. Des. **9**, 99 (2002).

[67] F. H. Stillinger and T. A. Weber, Phys. Rev. B **31**, 5262 (1985).

[68] P. Vashishta, R. K. Kalia, A. Nakano, W. Li, and I. Ebbsjö, in *Amorphous Insulators and Semiconductors*, edited by M. F. Thorpe and M. I. Mitkova, *NATO Advanced Study Institute*, Sub-Series 3 (Kluwer, Dordrooht), 1996, p. 151.

[69] P. Vashishta, R. K. Kalia, and I. Ebbsjö, Phys. Rev. Lett. **75**, 858 (1995); A. Nakano, R. K. Kalia, and P. Vashishta, *ibid.* **75**, 3138 (1995); R. K. Kalia, A. Nakano, K. Tsuruta, and P. Vashishta, *ibid.* **78**, 689 (1997); R. K. Kalia, A. Nakano, A. Omeltchenko, K. Tsuruta, and P. Vashishta, *ibid.* **78**, 2144 (1997).

[70] A. Y. Liu and M. L. Cohen, Phys. Rev. B **41**, 10727 (1990); G. L. Zhao and M. E. Bachlechner, Europhys. Lett. **37**, 287 (1997); G. L. Zhao and M. E. Bachlechner, Phys. Rev. B **58**, 1887 (1998).

[71] D. Cook, D. S. Malkus, and M. E. Plesha, *Concepts and Applications of Finite Element Analysis* (Wiley, New York, 1989).